PERGAMON

International Journal of Heat and Mass Transfer 44 (2001) 2751–2762

International Journal of HEAT and MASS TRANSFER

www.elsevier.com/locate/ijhmt

Numerical investigations of Lorentz force influenced Marangoni convection relevant to aluminum surface alloying

O. Velde *, R. Gritzki, R. Grundmann

Institute for Aerospace Engineering, Department of Mechanical Engineering, Dresden University of Technology, 01062 Dresden, Germany

Received 19 June 2000; received in revised form 3 August 2000

Abstract

This work deals with the numerical investigation of the development of a laser molten aluminum pool under the influence of static magnetic fields with different strengths. Special attention has been paid to laser surface alloying by means of nickel. It was observed that thermocapillary forces drive two counter-rotating vortices which by themselves induce two secondary vortices at the free surface. This scenario yields an alloyed layer with an extension of about half the maximum pool depth. In the presence of a static magnetic field applied perpendicular to the plane of interest, the system of vortices is suppressed. This damped flow situation in the melt results in a variation of the solute distribution in the solid and in shallower alloyed layers depending upon the applied magnetic induction.

Keywords: Finite element; Magneto-hydrodynamics; Solidification; Surface tension

1. Introduction

Today, corrosion and wear resistance as well as hard function layers on metal surfaces are produced by means of surface remelting, alloying and dispersing processes applying laser or electron beams as heat sources. Magnetofluid dynamics (MFD) might deliver a complementary process tool to have better control on the phenomena occurring in this kind of technology. With its aid processes may be devised to become more efficient and/or better surfaces can be developed since Lorentz forces can be applied to influence convection in a more appropriate way. But of course, the determination of all essential parameters remains a great challenge. The numerical investigation will give a better insight into the problem and will allow access today to hardly measurable or even non-measurable variables like temperatures or velocities within the melt. Moreover, parameter studies can be carried out fast and cheap, once a suitable numerical model has been developed.

Metal surface processing (see Fig. 1) is characterized by the application of a high density heat source like electron beam or laser. Since the majority of metals display a negative surface tension coefficient, temperature gradients at the free surface induce a thermocapillary-driven flow (Marangoni flow). It is directed from hot to cold.

From a modeler's point of view an electron beam – similar to the laser – can be represented by a surface related heat source because the electrons have a very small penetration depth before they exchange their kinetic energies with the material of impact [1]. Therefore, the literature dealing with both types of energy sources are discussed below.

Pirch et al. [2] have presented a three-dimensional model for the heat, momentum and solute transport in a one-step process of laser surface alloying. They have found an enhancement of solute in a certain depth of the melt pool dependent on the Marangoni flow pattern and the diffusion coefficient. Experimental and numerical investigations [3] of an electron beam surface alloying process of Ck45 (AISI 1045) with chromium showed the importance of the convective heat transfer on the melt pool geometry evolution if – as in the case of steel – the thermal conductivity is comparably small.

* Corresponding author. Tel.:+49-351-4638092; fax: +49-351-4638087.

E-mail address: velde@tfd.mw.tu-dresden.de (O. Velde).

0017-9310/01/$ - see front matter
PII: S0017-9310(00)00299-4

Nomenclature

c_p	specific heat at constant pressure
C	solute concentration
D	diffusion coefficient
det	determinant
e	element
f	volume force
g	earth acceleration
Δh_{melt}	latent heat
H	volumetric latent heat
j	current density
k	partition coefficient
K	curvature
l	length
m	mass flux
meas	geometric measure
p	pressure
P	power
q	volumetric heat source
r	characteristic radius
t	time
T	temperature
v	test function
w	velocity
x, y, z	coordinates

Greek symbols

Φ	dissipation function
φ	electric potential
γ	surface tension
δ	Kronecker symbol
Γ	boundary
η	dynamic viscosity
κ	thermal diffusivity
λ	thermal conductivity
Λ	temperature dependency of density
μ	permeability
ρ	density
σ_e	electric conductivity
τ	viscous stress tensor
Ω	domain

Subscripts and superscripts

l/s	liquid/solid
melt/Sol	melting/solidification
Surf	surface
n, t	normal/tangential
R	reference
$*$	dimensional

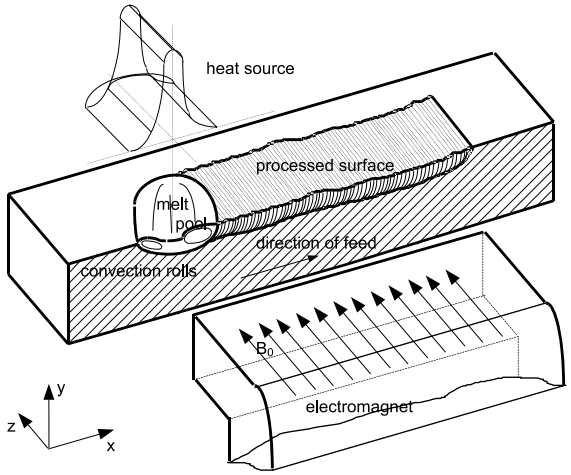

Fig. 1. Sketch of the physical domain.

So far, no publications concerning MFD accompanied surface treatment processes were found. In contrast, MFD applications in crystal growth processes are well reported. Static magnetic fields are used to suppress unsteady convection which produces inhomogeneity of the temperature and solute concentration, increasing thereby the quality of the crystal. A review is given by Hurle and Series [4]. On the contrary, rotating magnetic fields can control the convection by inducing fluid flow in a predefined way, such that an increase of the material transport can be reached [5,6].

Usually in surface remelting and alloying processes the surface is scanned by the heat source linearly and the produced tracks are then overlapped. In the case of long areas to be processed it is very difficult to handle a rotating magnetic field beneficially. Therefore, in this paper only a static magnetic field, see Fig. 1, is considered.

The influence of a static magnetic field upon the crystal growth of GaAs has been analyzed by Walker and Morthland [7]. They have considered magnetic field strengths of $B^* = 0.1$–10 T in whose presence the thermocapillary convection is confined to a thin layer at the surface leaving a quiescent inner core. Similar effects are expected if a static magnetic field is applied to influence the convection within the melt occurring during a surface alloying process.

2. Problem description

A Cartesian coordinate system is chosen such that its origin is attached to the center of the heat source. Hence, the specimen experiences a relative movement with the

velocity of feeding. A line like heat source is used which allows two-dimensional calculations neglecting derivatives in the z-direction. Alloyed layers are produced by conveying the pulverized material by means of a shielding gas into the melt.

The order of magnitude of the non-dimensional numbers (see Table 1) leads not necessarily to an a priori postulation of either laminar or turbulent movement in the melt pool. Above this, experimental investigations into these small-scale and high temperature convection cases are very rarely reported today. In the numerical investigation the flow is regarded laminar. The neglected mushy zone – although small in extension – tends to reduce the flow development since dendrites will grow in the liquid, which is again a fact that supports the assumption of a laminar regime.

The following assumptions have been made in order to obtain a realistic but yet feasible description of the problem:

- Compressibility is expressed by means of the Boussinesq approximation.
- All material properties are isotropic in both phases.
- A net heat flux is used to simulate the laser heating meaning that reflections and radiation are not considered separately as well as the cracking of the oxide layer.
- The material is opaque, i.e. the heat source can be treated surface related.
- The action of a shielding gas and free surface deformations are neglected.
- The magnetic induction within the melt is homogeneous.
- The alloy material reaching the surface is already molten.
- The solute (nickel) concentration is small enough to consider the mixture properties as being those of pure aluminum.

2.1. Governing equations

The governing equations, Eqs. (1)–(5), describing the transport mechanism of the processes involved consist of continuity, Navier–Stokes, energy, and concentration equations, respectively. Here, all material properties are assumed to be temperature independent although their temperature dependency will be taken into account in the numerical procedure later on.

$$\nabla \circ \mathbf{w} = 0, \tag{1}$$

$$\frac{\partial \mathbf{w}}{\partial t} + (\mathbf{w} \circ \nabla)\mathbf{w} = -\nabla p + \frac{1}{Re}\nabla^2 \mathbf{w} + \mathbf{e}_y \frac{Ra}{Pe\ Re} T + \mathbf{f}_L, \tag{2}$$

$$\frac{\partial T}{\partial t} + (\mathbf{w} \circ \nabla)T = \frac{1}{Pe}\nabla^2 T + \frac{Ec}{Re}\Phi + q_J + H(T), \tag{3}$$

$$\frac{\partial C}{\partial t} + (\mathbf{w} \circ \nabla)C = \frac{1}{Re\ Sc}\nabla^2 C. \tag{4}$$

Table 1
Values of the non-dimensional groups for aluminum

Non-dimensional group	Definition	Aluminum
Reynolds number	$Re = \frac{l_R \cdot w_R \cdot \rho}{\eta}$	2870
Prandtl number	$Pr = \frac{\eta}{\kappa\rho}$	0.007
Rayleigh number	$Ra = \frac{g l_R^3 \rho}{\kappa\eta} \frac{\Lambda}{\rho(T^*_{Sol})}(T^*_\infty - T^*_{Sol})$	40
Marangoni number	$Ma = \frac{l_R}{\eta\kappa} \frac{\partial\gamma}{\partial T}(T^*_\infty - T^*_{Sol})$	4300
Peclet number	$Pe = \frac{w_R \cdot l_R}{\kappa}$	20
Schmidt number	$Sc = \frac{\eta}{D\rho}$	65
Eckert number	$Ec = \frac{w_R^2}{(T^*_\infty - T_{Sol})c_p}$	2.2×10^{-6}
Magnetic Reynolds number	$Rm = \mu \cdot \sigma_e \cdot w_R \cdot l_R$	0.006
Hartmann number	$Ha = \sqrt{\frac{\sigma_e}{\eta}} B_0 \cdot l_R \quad (B_0 = 2T)$	160
Interaction parameter	$N = \frac{Ha^2}{Re}$	9

As the current flux must be free of divergence the equation for the electric potential is:

$$\nabla \circ \mathbf{j} = 0 = N[-\nabla^2\varphi + \nabla \circ (\mathbf{w} \times \mathbf{B})]. \quad (5)$$

The term $\mathbf{f_L}$ in Eq. (2) represents the Lorentz force induced by an external magnetic field $\mathbf{B}$. This is described by the following equation:

$$\mathbf{f_L} = \mathbf{j} \times \mathbf{B} = N(-\nabla \circ \varphi + \mathbf{w} \times \mathbf{B}) \times \mathbf{B}. \quad (6)$$

Eqs. (1)–(6) as well as the initial and boundary conditions have been non-dimensionalized by means of the similarity numbers defined in Table 1 and with:

$$\mathbf{w} = \frac{\mathbf{w}^*}{w_R}; \quad \begin{pmatrix} x \\ y \\ z \end{pmatrix} = \frac{1}{l_R}\begin{pmatrix} x^* \\ y^* \\ z^* \end{pmatrix}; \quad p = \frac{p^* l_R^2}{\rho_R w_R^2};$$
$$T = \frac{T^* - T_{Sol}}{\Delta T_R}; \quad t = \frac{t^* \cdot w_R}{l_R};$$
$$\mathbf{f_L} = \frac{\mathbf{f_L^*} l_R}{w_R^2}; \quad q = \frac{q^* l_R}{\rho_R c_p \Delta T_R w_R}; \quad \mathbf{j} = \frac{\mathbf{j}^* l_R B_0}{w_R^2 \rho_R};$$
$$\varphi = \frac{\varphi^*}{w_R B_0 l_R}; \quad \mathbf{B} = \frac{\mathbf{B}^*}{B_0}$$

Φ in Eq. (3) is the dissipation function which can be neglected compared to the high density heat source that is represented by $\hat{q}$, Eq. (7). A complementary reason for this assumption is the order of magnitude of the coefficient of the dissipation function, $Ec/Re \sim 10^{-9}$. The term, $q_J = Ec/N \cdot \mathbf{j}^2$, in Eq. (3) represents a volumetric heat source caused by Joule heating, whereas $H(T)$ represents the latent heat defined by Eq. (12). Due to this solution dependent source term the heat transfer Eq. (3) is an advection diffusion reaction equation in a mathematical sense which is not true for the Eqs. (4) and (5) which are an advection diffusion equation and a diffusion equation, respectively. The form of the Navier–Stokes equation (2) considered here is a two-dimensional advection diffusion reaction equation as the Lorentz force is solution (i.e. velocity) dependent too.

2.2. Initial and boundary conditions

A specimen with the dimensions of 100×20 mm is considered. Its velocity is the feeding velocity in the solid state as well as at the melting and resolidification fronts, i.e.

$$\mathbf{w} = (\, w_{feed} \quad 0 \quad 0 \,)^T.$$

Its initial temperature is that of the environment,

$$T_0 = \frac{293\ \mathrm{K} - T_{Sol}}{\Delta T_R}.$$

The heat flux distribution over the surface is described by a Gaussian-type equation, Eq. (7), where r is the characteristic radius and P is the source power that effectively enters the material. The width of a line like deformed source is d.

$$\hat{q}(x,z) = P\frac{1}{d\sqrt{2\pi}r}\exp\left(-\frac{x^2}{2r^2}\right) \quad (7)$$

While carrying out the numerical procedure it was found that heat losses of the specimen into ambience have very little impact on melt dynamics due to the short interval ($\Delta t^* = 0.5$ s) considered here. Hence, the boundaries of the specimen can be treated adiabatically, Eq. (8).

$$\nabla T \circ \mathbf{n} = 0 \quad (8)$$

The force balance at the free deformable surface is described by the following equation, with ∇_{Surf} the surface (i.e. tangential) gradient:

$$(\tau - p\delta) \circ \mathbf{n} = (2\gamma K - p_a)\mathbf{n} + \nabla_{Surf}\gamma \quad (9)$$

In the numerical simulation free surface deformations and shielding gas interaction with the molten surface are neglected. Therefore, only the tangential part of Eq. (9) is incorporated in the numerical procedure, i.e. Eq. (15). The specimen is treated electrically insulated and no outer electric field is applied. Therefore, the surface of the specimen experiences a von Neumann boundary condition, Eq. (10):

$$\nabla\varphi \circ \mathbf{n} = (\mathbf{w} \times \mathbf{B}) \circ \mathbf{n} \quad (10)$$

Throughout this work the magnetic field will be treated as homogeneous. Hence, a magnetic induction, $\mathbf{B} = (\,0 \quad 0 \quad 1\,)^T$, is applied.

To produce a low alloyed layer a mass flux of nickel ($\rho_{Ni}(T_{Sol}) = 7900$ kg/m^3) over the molten surface according to Table 3 is applied. A species flux balance at the resolidification front in the normal direction yields with w_{Sol} the solidification speed, Eq. (11):

$$C_l w_{Sol}(k-1) = -\frac{1}{Re\ Sc}\nabla C_l \circ \mathbf{n} \quad (11)$$

The basic non-dimensional numbers characterizing the fluid flow problem are the Reynolds number (ratio of inertial and viscous forces), the Prandtl number (ratio of viscosity and conductivity of a fluid), the Rayleigh number (ratio of buoyant and viscous forces), the Marangoni number (ratio of thermocapillary and viscous forces), the Peclet number (ratio of characteristic pool length and heat penetration depth) and the Schmidt number (ratio of viscosity and mass diffusivity). The definitions are listed in Table 1.

Hereby, w_R is a characteristic velocity, i.e. the maximum velocity at the surface. Based on experimental observations the characteristic melt pool dimension is about $l_R = 1$ mm. The maximum speed at the surface of the melt puddle is of the order of 1 m/s, see [2,3]. The material properties reported in Table 2 are fixed for a

Table 2
Material properties of aluminum

Property of aluminum	Reference
$\gamma(T) = 0.914\ \mathrm{N/m} - 0.35 \times 10^{-3}\mathrm{N/m\ K}(T - T_{\mathrm{Sol}})$	Iida and Guthrie [16]
$\eta(T) = 0.1492 \times 10^{-3}\exp\left\{\frac{(16500\ \mathrm{J/mol}}{8.3144\ (\mathrm{J/mol\ K}) \cdot T}\right\}\mathrm{Pa\ s}$	Brandes [18]
$\lambda_{\mathrm{s}}(T) = 197\ \mathrm{W/m\ K} - 6.39 \times 10^{-3}\ \mathrm{W/m\ K^2}(T - T_{\mathrm{Sol}})$	Touloukian [19]
$\lambda_{\mathrm{l}}(T) = 94\ \mathrm{W/m\ K} + 0.333 \times 10^{-3}\ \mathrm{W/m\ K^2}(T - T_{\mathrm{Sol}})$	Brandes [18]
$\mu = 1$	Moreau [8]
$\rho(T_{\mathrm{Sol}}) = 2380\ \mathrm{kg/m^3}$	Iida and Guthrie [16]
$\Lambda = -0.35\ \mathrm{kg/m^3\ K}$	Iida and Guthrie [16]
$\sigma_{\mathrm{es}} = 3.5 \times 10^7\ 1/\Omega\mathrm{m}$	DUBBEL [20]
$\sigma_{\mathrm{el}} = 5.0 \times 10^6\ 1/\Omega\mathrm{m}$	Moreau [8]
$c_{\mathrm{ps}} = 945\ \mathrm{J/kg\ K};\quad \Delta h_{\mathrm{melt}} = 355.9 \times 10^3\ \mathrm{J/kg}$	DUBBEL [20]
$c_{\mathrm{pl}} = 858\ \mathrm{J/kg\ K}$	Iida and Guthrie [16]
$T_{\mathrm{Sol}} = 933\ \mathrm{K}$	Iida and Guthrie [16]

temperature of $T^* = 1200$ K. The Marangoni number is more appropriate than the Reynolds number for surface tension driven flows. For the Marangoni number calculation a temperature difference of 500 K has been applied.

In terms of MFD the basic non-dimensional numbers read as follows: magnetic Reynolds number (ratio of induced and applied magnetic field strength), Hartmann number (ratio of electromagnetic volume forces and viscous forces) and interaction parameter (ratio of electromagnetic volume forces and inertial forces). These parameters have been calculated with a magnetic induction of $B_0 = 2$ T, a value that can be reached with electromagnets in a laboratory scale.

All material properties concerned here and in the numerical program were those of aluminum 99.99%. The temperature-dependent material properties are listed in Table 2. Since phase transformations take place, material properties change not always continuously with temperature. These discontinuities occur at the Curie point or at liquidus.

Buoyancy is dominated by thermocapillarity in these kinds of problems as two orders of magnitudes lie between Marangoni and Rayleigh numbers. Therefore, the influence of the latter has been neglected and the buoyancy term was not incorporated in the numerical procedure.

Since $Rm \ll 1$ convection has a negligible influence on the magnetic field because the magnetic field strength – induced by the fluid motion – is small compared to the applied magnetic field strength, see Moreau [8]. Hence, a homogeneous and steady magnetic flux, **B**, is considered in this work. An interaction parameter of ca. 10 (Table 1) means that the convection can be influenced considerably by an external magnetic field.

A crucial point in calculating melting and resolidifying problems is the treatment of the phase transition front. This has been done by employing an effective viscosity distribution. Beneath the melting temperature the viscosity has values which are six orders of magnitudes higher than the real liquid values. Above liquidus the temperature dependency of viscosity according to Table 2 is considered.

It was found that the application of an effective specific heat approach for the latent heat of fusion is very grid and time step dependent. Hereby the specific heat is calculated from an enthalpy temperature curve. In contrast, the latent heat is modeled as a sink and source, respectively, in Eq. (3). For a given two-dimensional element passed by the isotherm of solidification, the latent heat release is given by Eq. (12),

$$H = \frac{\Delta h_{\mathrm{melt}} w_{\mathrm{Sol}} b \rho}{\frac{1}{2}\det(e)\Delta t} \tag{12}$$

From this equation the condition raises that the local solidification front, having a local length b, see Fig. 2, may not travel far beyond the element border. Mathematically, this is expressed by, $w_{\mathrm{Sol}} \cdot \Delta t \ll \mathrm{meas}(e)$, which sets limitations for both the time step as well as for the grid generation.

As the solute is rejected at the solidification front with a certain ratio, $C_{\mathrm{s}} = k \cdot C_{\mathrm{l}}$, see e.g. Kurz and Fischer [9], an appropriate flux condition has to be incorporated in the numerical procedure. Therefore, for each element accommodating the solidification front the following procedure is applied, Fig. 3. The mass conservation of solute is expressed by Eq. (13),

$$\int_e C^{\mathrm{old}}(n)\,\mathrm{d}n = \int_e C^{\mathrm{new}}(n)\,\mathrm{d}n \tag{13}$$

and by the condition of a constant derivative of the solute concentration in the tangential direction. This together with the above-mentioned ratio $C_{\mathrm{l}}/C_{\mathrm{s}}$ yields a

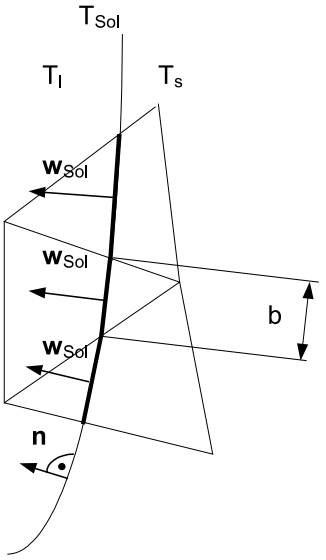

Fig. 2. Elementwise isotherm of solidification.

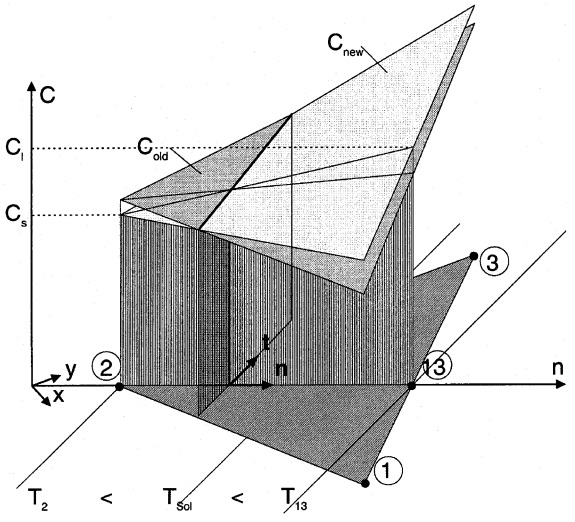

Fig. 3. Concentration distribution in an element.

new concentration distribution within an element. Obviously, this results in a pile up of solute right before solidification. The superscripts, old and new, in Eq. (13) describe the solute concentration before and after the application of the flux condition.

Apparently, the local parameter ($Re \cdot Sc = w_{\mathrm{Sol}} \cdot \Delta n/D$) is crucial because of the small order of magnitude ($\sim 5 \times 10^{-9}$ m^2/s, see [16]) of liquid diffusivity in metals. Hence, Eq. (4) is much more dominated by convection than all the other conservation equations. To reach a convergent solution of the solute transport Eq. (4) a ten times higher mass diffusivity, $D = 5 \times 10^{-8}$ m^2/s, was used in the calculations as done by Pirch [17]. When using a factor of 15, he showed that the maximal solute concentration at the resolidification front decreases by about 6%, whereas the location (i.e. the distance from the surface) of this value increases by about 20%. These deviations, however, will not affect the main purpose of this work. A further grid refinement would have led to convergence even with the actual mass diffusivity but would have increased the necessary CPU time considerably.

In general, the temperature dependent properties (Table 2) were treated as being constant within an element. This approach turned out to be realistic as long as the grid has been fine enough in regions with high temperature gradients.

3. Numerical procedure and its implementation

The incorporation of boundary conditions in a finite element formulation (or more precise in a variational formulation) reveals the flexibility of the finite element method (FEM). To prove this, the variational formulation of the steady version of the Navier–Stokes equations (2), is discussed in detail. Multiplying the stress tensor term by the test function, $\mathbf{v}$, and integrating the result partially, yields the following boundary integral:

$$\int_{\Omega} \nabla \circ \tau \circ \mathbf{v}\,\mathrm{d}\Omega = -\int_{\Omega} \tau^{\circ}_{\circ}(\nabla \mathbf{v})^{\mathrm{T}}\,\mathrm{d}\Omega + \int_{\Gamma} \mathbf{n} \circ \tau \circ \mathbf{v}\,\mathrm{d}\Gamma. \tag{14}$$

Here, the viscous stress tensor is defined by $\tau = v(\nabla \mathbf{w} + (\nabla \mathbf{w})^{\mathrm{T}})$. For a mathematically detailed definition of functions and function spaces the reader is referred to Carey and Oden [10]. Now, it is possible to use the boundary integrals to formulate boundary conditions in a natural way. Using the tangential part of Eq. (9) under the assumption of neglected curvature the Marangoni boundary condition along the boundary Γ is:

$$\tau_t = -\nabla_{\mathrm{Surf}}\gamma = ((\mathbf{n} \circ \tau \circ \mathbf{n})\mathbf{n} - \mathbf{n} \circ \tau) \tag{15}$$

and by this variational formulation of the momentum equation finally reads:

$$\begin{aligned}\int_{\Omega}(\mathbf{w} \circ \nabla)\mathbf{w} \circ \mathbf{v}\,\mathrm{d}\Omega = &-\int_{\Omega} \nabla p \circ \mathbf{v}\,\mathrm{d}\Omega - \int_{\Omega} \tau^{\circ}_{\circ}(\nabla \mathbf{v})^{\mathrm{T}}\,\mathrm{d}\Omega \\ &+ \int_{\Gamma}(\mathbf{n} \circ \tau \circ \mathbf{n})\mathbf{n}\,\mathrm{d}\Gamma + \int_{\Gamma} \nabla\gamma \circ \mathbf{n}\,\mathrm{d}\Gamma + \int_{\Omega} \mathbf{f} \circ \mathbf{v}\,\mathrm{d}\Omega.\end{aligned} \tag{16}$$

This controls, that also the Marangoni boundary condition along the boundary Γ is included in the variational formulation. In Eq. (16), $\mathbf{f}$ stands for any kind of volume force.

The Marangoni boundary condition was implemented in the finite element code ParallelNS, a public

domain research code of the Dresden University of Technology and the University of Göttingen. This code was originally developed for testing a non-overlapping domain decomposition method, see Auge et al. [11], Lube et al. [12]. It works with a stabilized FEM because standard methods are not suitable for calculating convection dominated flows. The method is called Galerkin-least-squares FEM and includes stabilization to overcome problems resulting from convection and velocity pressure coupling, Hughes et al. [13,14]. The basic concept of the least-squares FEM can be used for a wide range of applications, [15]. Linear test function and triangular elements are used in the model exclusively.

As all equations are solved in the whole computational domain, some means to save CPU time are applied for solving the Navier–Stokes-equations (2). The velocity vector is known a priori throughout the calculations if temperatures are below liquidus. In those regions the coefficients of the stiffness matrix along with the solution vector obtain suitable values.

4. Results

4.1. Laser alloying without a magnetic field

The thermal boundary conditions have been chosen to allow the development of a melt pool with a perimeter of about 3 mm. Therefore, a net heat flux according to Table 3 is applied. In terms of the thickness of the alloyed layer a quasi-steady status is reached after $t = 250$, see Fig. 9. Hence, the process time to be investigated was, $t = 500$, which refers to $t^* = 0.5s$. Due to this relatively short time, all solid body boundary conditions could be realistically described as adiabatic, at least till $t = 450$ (Fig. 4). A constant feeding velocity, $w_{\text{feed}} = 0.01$, was prescribed.

Table 3
Applied boundary conditions

Variable	Annotation
$P^* = 2.0$ kW	According to Eq. (7)
$d^* = 10.0$ mm	According to Eq. (7)
$r^* = 0.4$ mm	According to Eq. (7)
$m^* = 0.225$ kg/m^{2}s	
$w^*_{\text{feed}} = 0.01$ m/s	

The development of the melt pool geometry is regular since the enthalpy transport within the melt is almost entirely diffusive. This is caused by the high thermal diffusivity of aluminum. The melt puddle shows a nearly symmetric shape around an axis which moves with the feeding velocity away from its initial position at the laser axis, Fig. 4. Even at locations where high velocities prevail, convective heat transfer has only very little influence on the evolution of the solidification front.

When the process approaches the quasi-steady-state an alloyed layer can move considerably beyond the solidification front. Otherwise the local solidification velocity exceeds the feeding velocity to such an extent that the solute is trapped within the melt.

The flow field is determined by two counter-rotating primary vortices right below the surface. They are induced by thermocapillary forces. After a certain time ($t \sim 70$) these Marangoni vortices start to induce secondary vortices beneath, of course again counter-rotating. The vortex pattern in the form of stream traces is displayed in Fig. 5, showing the four vortices in the melt. Most of the particles moving through the liquid resolidify close to the surface of the specimen. This feature is also highlighted by the concentration distribution in the processed material. As the process carries on above the point of quasi-steadiness the secondary vortices grow and the downstream vortex eventually becomes dominant, Figs. 6 and 7. At $t = 300$, a maximum speed at the free surface of $w_{max} = 1.05$ is reached.

The solute is almost entirely transported by convection. Therefore, the behavior of the Marangoni vortex at the solidification front will lead to the frozen solute distribution, see Figs. 8 and 9. The solution of Eq. (4) visualizes the current flow situation due to the convection dominance.

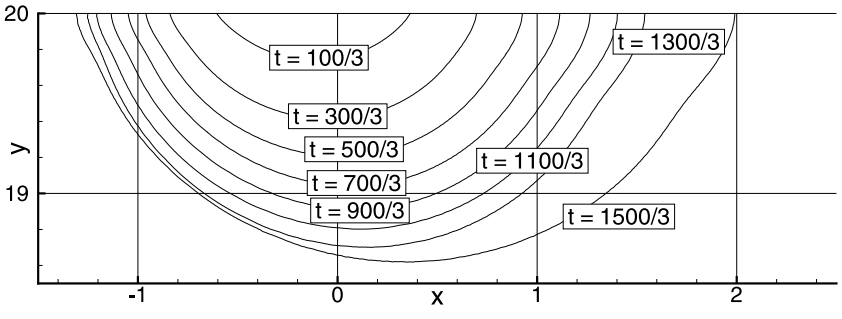

Fig. 4. Solidification isotherm development with time.

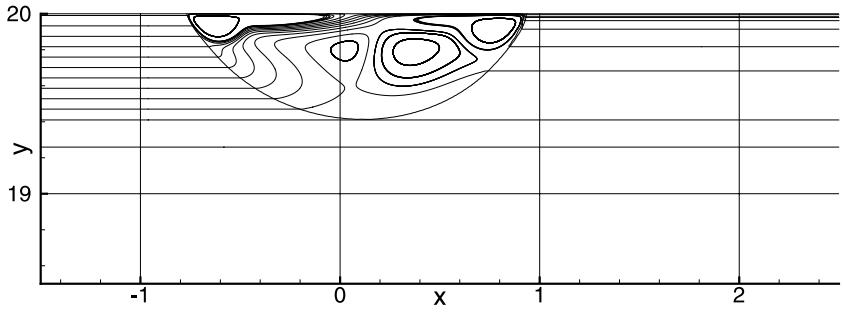

Fig. 5. Stream traces at $t^* = 0.1$ s.

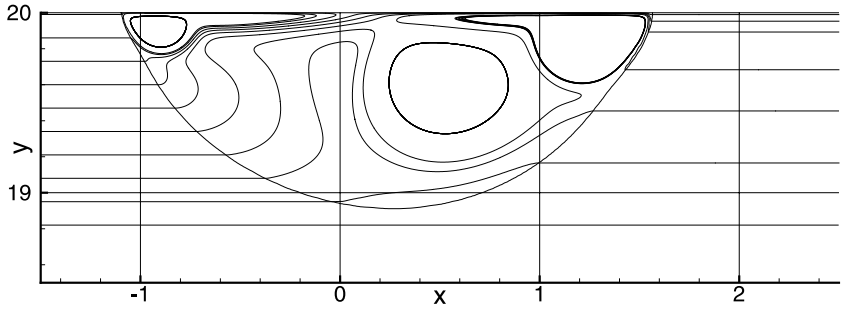

Fig. 6. Stream traces at $t^* = 0.3$ s.

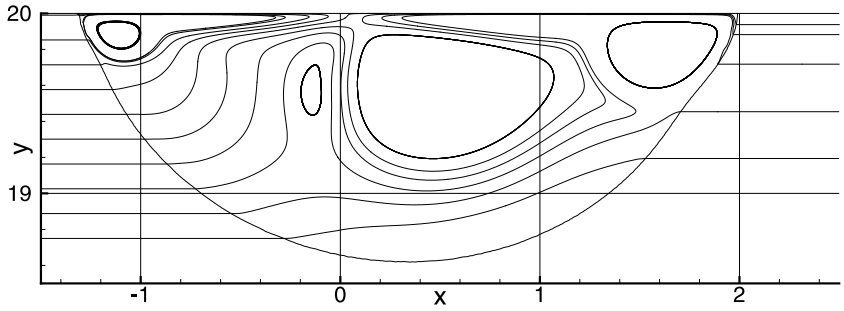

Fig. 7. Stream traces at $t^* = 0.5$ s.

4.2. Laser alloying with a magnetic field

In the numerical program five different values of the magnetic induction were considered which are $B^* = 0.25$, 0.5, 0.75, 1.0, and 2.0 T.

$B^* = 0.5$ T: The pool geometry is enlarged and the secondary vortices are almost entirely suppressed by the Lorentz forces, compare Figs. 7 and 10. The solute distribution within the alloyed layer has changed considerably although the depth of this layer is hardly altered, see Fig. 8, Figs. 11 and 17.

$B^* = 0.75$ T: The melt pool geometry is again enlarged and the secondary vortices are totally vanished, see Fig. 12. The downstream Marangoni vortex is widened but its momentum is lowered such that the mass transport is less intense and the solute density in the solid is decreased, Fig. 17.

$B^* = 2.0$ T: The results of this case are discussed in greater detail because here the highest magnetic field strength in the present work was considered. Joule heating has remarkable influence on the pool geometry development, compare Figs. 4 and 13. Especially at the resolidification front it leads to an enlargement of the melt pool.

Since Lorentz forces are directed against their causes, the flow is decelerated and stratified perpendicular to the

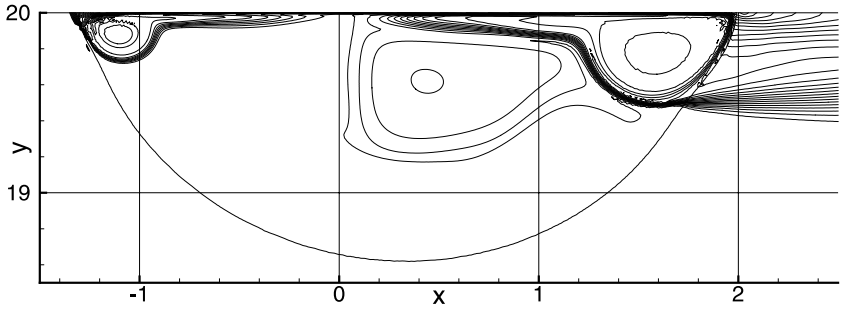

Fig. 8. Solute concentration at $t^* = 0.5$ s.

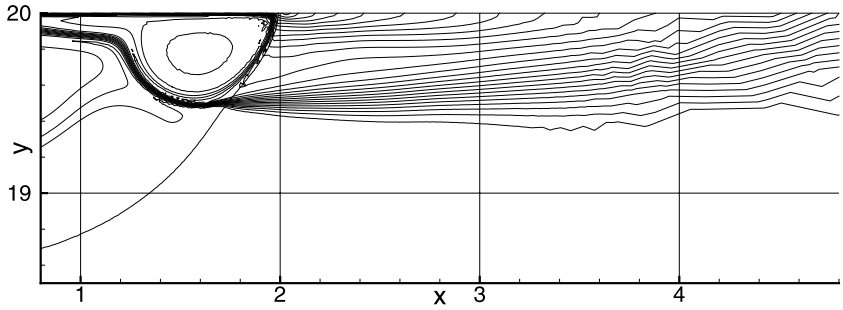

Fig. 9. Solute concentration in the solid at $t^* = 0.5$ s.

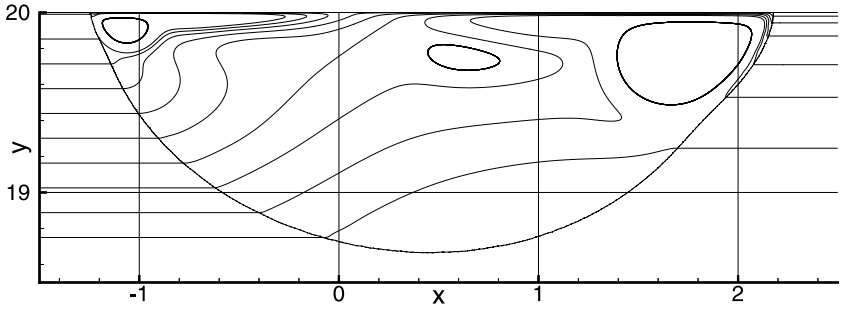

Fig. 10. Stream trace at $t^* = 0.5$ s, $B^* = 0.5$ T.

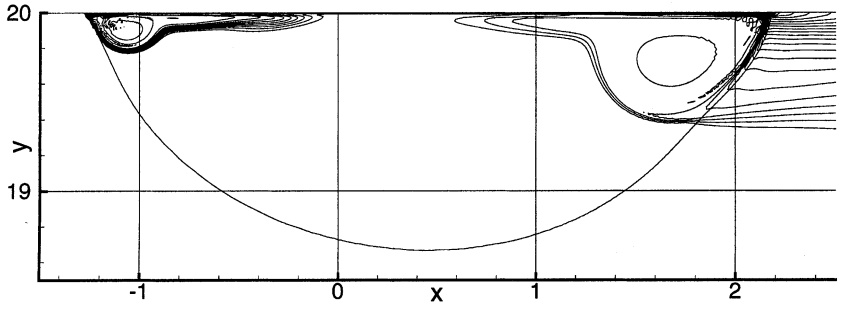

Fig. 11. Solute concentration at $t^* = 0.5$ s, $B^* = 0.5$ T.

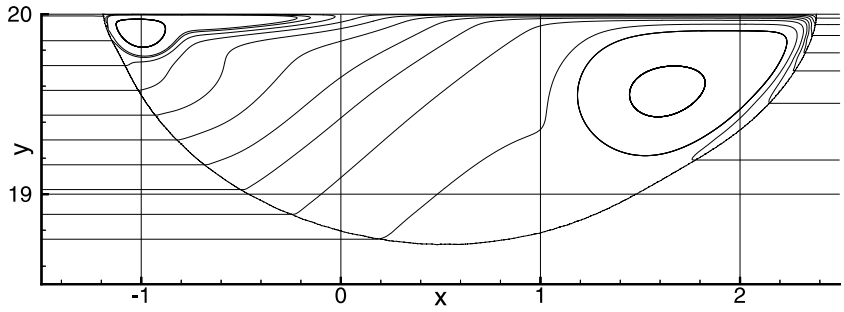

Fig. 12. Stream trace at $t^* = 0.5$ s, $B^* = 0.75$ T.

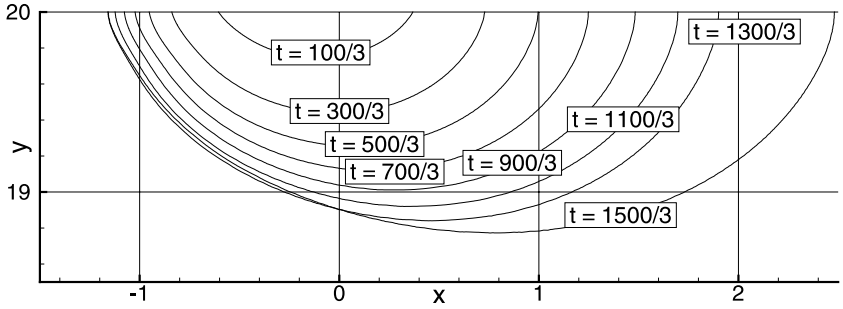

Fig. 13. Solidification isotherm development with time, $B^* = 2$ T.

direction of feed, Fig. 14. The Lorentz forces let the secondary eddies totally vanish and also suppress the Marangoni vortices. The maximum speed at the surface does not exceed the value of $w_{max} = 0.85$. At the heated surface close to resolidification front the tangential temperature gradients are not high enough to induce velocities higher than $w_{max} = 0.6$. This yields a momentum that is not strong enough to overcome the Lorentz forces to such an extent that a vortex can be established, Fig. 14. Therefore, the mass transfer into deeper regions of the melt is decreased and a very shallow alloyed layer is obtained, Fig. 15.

The electric potential within the melt has values between $\varphi = 0.0$ and 0.2 mV, qualitatively shown in Fig. 16. The sharp changes in the isolines of the electric potential at the melt isotherm are due to the temperature dependency of the electrical conductivity of aluminum.

Drawing the solute distribution of all investigated cases at a certain location, $x = 2.6$, into one diagram illustrates best the potential being in this MFD application, Fig. 17.

5. Conclusion

The calculations of the melt pool development in a strictly transient framework revealed the convection dominated nature of the solute transport in this kind of

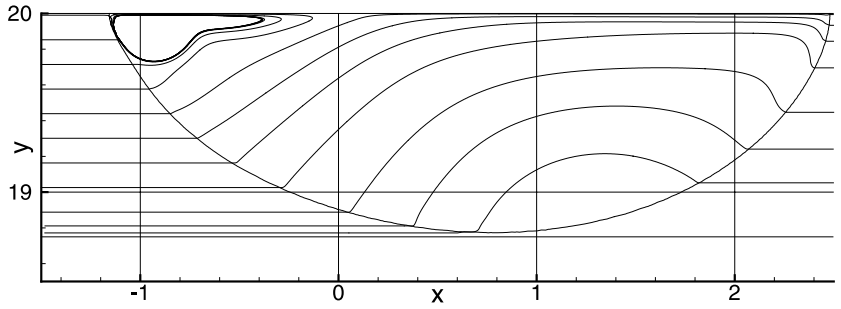

Fig. 14. Stream traces at $t^* = 0.5$ s, $B^* = 2$ T.

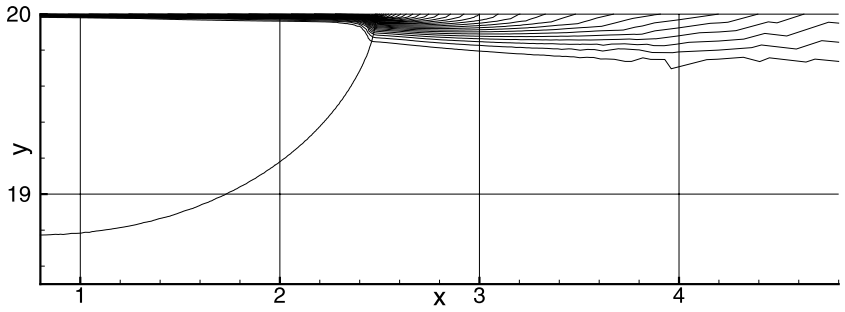

Fig. 15. Solute concentration at $t^* = 0.5$ s, $B^* = 2$ T.

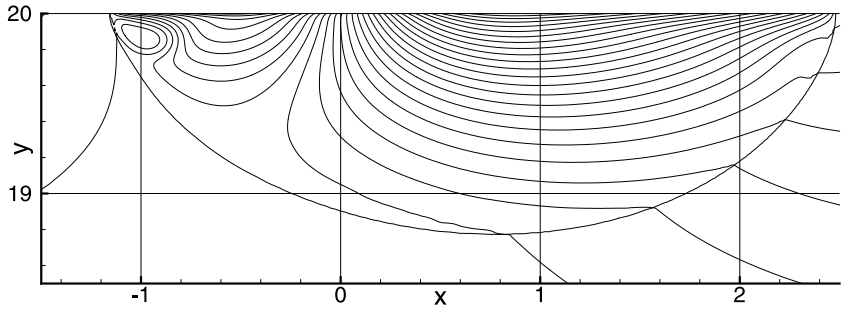

Fig. 16. Electric potential at $t^* = 0.5$ s, $B^* = 2$ T.

surface flow problem. After an initial startup the final pool geometry will establish and the flow structure leads to a solute distribution in the solid. Beyond this stage, the solute concentration in the solid approaches some constant state with an alloyed layer of almost half the pool depth, Fig. 9.

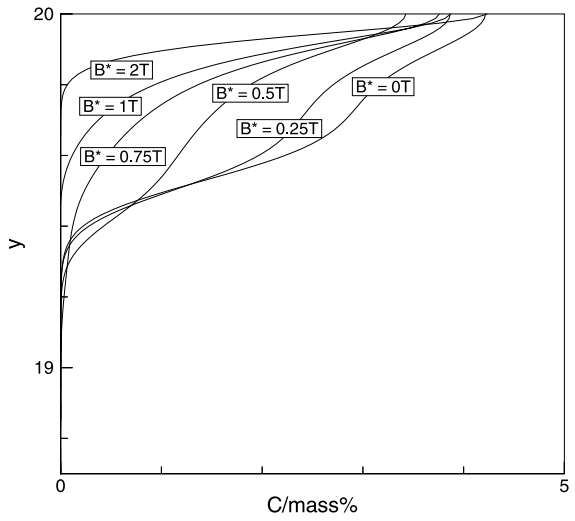

Fig. 17. Solute concentration distribution (mass%) at $x = 2.6$.

It could be shown that Marangoni vortices at the free surface induce counter-rotating secondary vortices right beneath. The primary vortices are fast turning and flat. Portions of the primary and secondary vortices will be suppressed with increasing magnetic induction and the latter will entirely vanish if the magnetic field strength is higher than $B^* = 0.5$ T.

A static magnetic field applied to add damping volume forces, i.e. Lorentz forces, can calm the flow by suppressing vortices and lowering the velocities at the free surface. Therefore, the mixing of the solute will be of course less intense and the depth of the alloyed layer will be smaller.

Thinking of the utilization of magnetic fields in an industrial process the applied magnetic induction would be certainly smaller than the maximum considered in the numerical analysis. This will decrease the alloying depth lesser. Since the proposed magnetic induction for influencing the alloying of aluminum surfaces is smaller than 2.0 T, comparable cheap electromagnets – certainly water-cooled – can be used in an industrial process.

The external magnetic field stabilizes the free surface avoiding therefore, the splashing of the molten material. This allows the application of laser beams with higher power, higher feeding velocities and hence higher throughput rates. The suppressed splashing would also allow the alloying of material which has a melting point

much higher than that of aluminum. Combining magnetic induction, beam power and rate of feed reasonably will result in higher productivity and certainly in deeper alloyed layers.

Apparently, the extreme of the investigated cases ($B^* = 2.0$ T) does not yield alloyed layers which are desirable from a manufacturer's point of view. Anyway, this has not been the major intention of this paper. The purpose was more to show the possibilities lying in the application of MFD to surface treatment technologies.

Acknowledgements

This work was supported by the Deutsche Forschungsgemeinschaft in the framework of the "Innovationskolleg Magnetofluiddynamik elektrisch leitfähiger Flüssigkeiten" under the Contract No.INK18/B2-1.

References

[1] S. Schiller, U. Heisig, S. Panzer, Electron Beam Technology, Wiley, New York, 1982, p. 33.
[2] N. Pirch, E.W. Kreutz, X. He, B. Mordike, 3D modeling of heat, momentum and solute transport in laser surface alloying, in: Proceedings of VIII Conference on Modelling of Casting, Welding and Advanced Solidification Processes, TMS Publications, 1998, pp. 329–336.
[3] O. Velde, F. Rüdiger, R. Grundmann, Theoretical and experimental investigations of electron beam surface remelting and alloying, Metall. Trans. B 31B (2000) 1405–1417.
[4] D.T.J. Hurle, R.W. Series, in: D.T.J. Hurle (Ed.), Handbook of Crystal Growth, vol. 2, North-Holland, Amsterdam, 1994, p. 259 (chapter 5).
[5] R.U. Barz, G. Gerbeth, U. Wunderwald, E. Buhrig, Yu.M. Gelfgat, Modelling of the isothermal melt flow due to rotating magnetic fields in crystal growth, J. Cryst. Growth 180 (1997) 410–421.
[6] K.H Spitzer, Application of rotating magnetic fields in czochalski crystal growth, Progress in Crystal Growth and Characterization of Materials, 1999, pp. 39–58.
[7] T.E. Morthland, J.S. Walker, Convective heat transfer due to thermocapillary convection with a strong magnetic field parallel to the free surface, Int. J. Heat Mass Transfer 40 (1997) 3283–3291.
[8] R. Moreau, Magnetohydrodynamics, Kluwer Academic Publishers, Dordrecht, Netherlands, 1990.
[9] W. Kurz, D.J. Fischer, Fundamentals of Solidification, third ed., Trans Tech Publication, Switzerland, 1992.
[10] G.O. Carey, J.T. Oden, Finite Elements: Fluid Mechanics, Volume VI of the Texas Finite Element Series, Prentice-Hall, Englewood Cliffs, New Jersey, 1986.
[11] A. Auge, A. Kapurkin, G. Lube, F.-C. Otto, A note on domain decomposition of singulary perturbed elliptic problems, in: Proceedings of the Ninth International Conference on Domain Decomposition Methods, Wiley, New York, 1998.
[12] G. Lube, F.-C. Otto, H. Müller, A non-overlapping domain decomposition method for parabolic initial-boundary value problems, Appl. Numer. Math. 28 (1998) 359–369.
[13] T.J.R. Hughes, L.P. Franca, M.A. Balestra, New finite element formulation for computational fluid dynamics: V. Circumventing the Babuska–Brezzi condition: a stable Petrov–Galerkin formulation of the Stokes problem accommodating equal-order interpolations, Comput. Meth. Appl. Mech. Eng. 59 (1986) 85–99.
[14] T.J.R. Hughes, L.P. Franca, G.M. Hulbert, A new finite element formulation for computational fluid dynamics: VIII. The Galerkin/least-squares method for advective–diffusive equations, Comput. Meth Appl. Mech. Eng. 73 (1989) 173–189.
[15] B. Jiang, The Least-Squares Finite Element Method, Springer, Berlin, Heidelberg, 1998.
[16] T. Iida, R.I.L. Guthrie, The Physical Properties of Liquid Metals, Clarendon Press, Oxford, 1988.
[17] N. Pirch, Randschichtlegieren von Aluminiumwerkstoffen mit Laserstrahlung: Physikalische Prozesse, Modelle und Integrationsverfahren, Ph.D. Thesis, RWTH Aachen, Germany, 1995, p. 12.
[18] E.A. Brandes, Smithell's Metals Reference Book, sixth ed., Butterworth, Guildford, UK, 1983.
[19] Y.S. Touloukian, R.W. Powell, C.Y. Ho, P.G. Klemens, Thermal conductivity of metallic elements and alloys, Thermophysical Properties of Matter 1 (1970) 1–9.
[20] W. Beitz, K.-H. Küttner (Eds.), DUBBEL Taschenbuch für den Maschinenbau, eighteenth ed., Springer, Berlin, Heidelberg, New York, 1994, pp. D43–D47.